Anisotropic Tomography Around La Réunion Island From Rayleigh Waves

Alessandro Mazzullo, Eléonore Stutzmann, Jean-Paul Montagner, Sergey Kiselev, Satish Maurya, Guilhem Barruol, Karin Sigloch

▶ **To cite this version:**

Alessandro Mazzullo, Eléonore Stutzmann, Jean-Paul Montagner, Sergey Kiselev, Satish Maurya, et al.. Anisotropic Tomography Around La Réunion Island From Rayleigh Waves. Journal of Geophysical Research : Solid Earth, 2017, 10.1002/2017JB014354 . hal-01640504

HAL Id: hal-01640504

https://hal.univ-reunion.fr/hal-01640504

Submitted on 21 Nov 2017

HAL is a multi-disciplinary open access archive for the deposit and dissemination of scientific research documents, whether they are published or not. The documents may come from teaching and research institutions in France or abroad, or from public or private research centers.

L'archive ouverte pluridisciplinaire **HAL**, est destinée au dépôt et à la diffusion de documents scientifiques de niveau recherche, publiés ou non, émanant des établissements d'enseignement et de recherche français ou étrangers, des laboratoires publics ou privés.

AGU PUBLICATIONS

JGR

Journal of Geophysical Research: Solid Earth

RESEARCH ARTICLE
10.1002/2017JB014354

Anisotropic Tomography Around La Réunion Island From Rayleigh Waves

Alessandro Mazzullo[1], Eléonore Stutzmann[1], Jean-Paul Montagner[1], Sergey Kiselev[2], Satish Maurya[1], Guilhem Barruol[1,3], and Karin Sigloch[4]

[1]Institut de Physique du Globe de Paris, Sorbonne Paris Cité, CNRS UMR 7154, Paris, France, [2]Institute of Physics of the Earth, Moscow, Russia, [3]Laboratoire de Geosciences, Universite de La Réunion, Institut de Physique du Globe de Paris, Sorbonne Paris Cité, CNRS UMR 7154, Saint-Denis, France, [4]Department of Earth Sciences, University of Oxford, Oxford, UK

Key Points:
- A new high-resolution 3-D anisotropic *S* wave velocity model of the western Indian Ocean is obtained using OBS and land stations
- A shallow east-west slow velocity anomaly beneath the Rodrigues Ridge connects Reunion upwelling and the Central Indian Ridge
- The Reunion slow velocity signature is connected at depth with a large slow velocity zone observed beneath the entire Mascarene Basin

Supporting Information:
- Supporting Information S1

Correspondence to:
E. Stutzmann,
stutz@ipgp.fr

Citation:
Mazzullo, A., Stutzmann, E., Montagner, J.-P., Kiselev, S., Maurya, S., Barruol, G., & Sigloch, K. (2017). Anisotropic tomography around Réunion Island from Rayleigh waves. *Journal of Geophysical Research: Solid Earth*, *122*. https://doi.org/10.1002/2017JB014354

Received 26 APR 2017
Accepted 11 OCT 2017
Accepted article online 25 OCT 2017

©2017. American Geophysical Union. All Rights Reserved.

Abstract In the western Indian Ocean, the Réunion hot spot is one of the most active volcanoes on Earth. Temporal interactions between ridges and plumes have shaped the structure of the zone. This study investigates the mantle structure using data from the Réunion Hotspot and Upper Mantle-Réunions Unterer Mantel (RHUM-RUM) project, which significantly increased the seismic coverage of the western part of the Indian Ocean. For more than 1 year, 57 ocean bottom seismometer stations and 23 temporary land stations were deployed over this area. For each earthquake station path, the Rayleigh wave fundamental mode phase velocities were measured for the periods from 30 s to 300 s and group velocities for the period from 16 s to 250 s. A three-dimensional model of the shear velocity in the upper mantle was built in two steps. First, the path mean phase and group velocities were inverted, to obtain regionalized velocity maps for each separate period. Then, all of the phase and group velocity maps were combined and inverted at each grid point, to obtain the local *S* wave velocity as a function of depth, using a transdimensional inversion scheme. The three-dimensional anisotropic *S* wave velocity model has resolution down to 300 km in depth. The tomographic model and surface tectonics are correlated down to ~100 km in depth. Starting at 50 km in depth, a slow velocity anomaly beneath Rodrigues Ridge and the east-west orientation of the azimuthal anisotropy show a connection between Réunion upwelling and the Central Indian Ridge. The slow velocity signature beneath La Réunion is connected at greater depths (150–300 km) with a large slow velocity zone beneath the entire Mascarene Basin. This develops along a northeast direction, following the general motion direction of the African Plate. These observations indicate nonisotropic spreading of hot plume material and dominant horizontal flow in the upper mantle beneath this area.

1. Introduction

Hot spots are basaltic (volcanic) regions that appear to be the surface expression of rising mantle plumes. Plumes are associated with various geodynamic and geophysical processes, such as intraplate volcanism, massive flood basalt provinces, and volcanic chain islands, and they have an important geodynamic role in the evolution of continental breakup (Courtillot et al., 1999). The Réunion hot spot has well-defined characteristics and is classified as a "primary" plume (i.e., initial igneous province, intraplate volcano, age progression of volcanoes along a linear chain, swell, and geochemical anomaly) (Courtillot et al., 2003, 1986; Morgan, 1971, 1978; Nataf, 2000; Seton et al., 2012).

This hypothesis is supported by dating and geodynamic reconstructions, and geochemical and magnetic studies (Duncan et al., 1990; Duncan & Hargraves, 1990; Georgen et al., 2001; Seton et al., 2012; Storey, 1995).

However, the nature and origin at depth of the Réunion hot spot are still controversial, and some geological structures observed in this area have indicated additional complexity in the general understanding of the evolution of this hot spot track. The volcanic Rodrigues Island (Figure 1), for example, has been dated to 1.5 Ma (McDougall, 1965) but does not lie along this apparent hot spot trail; instead, Rodrigues Island is located on the volcanic Rodrigues Ridge that was proposed by Morgan (1978) to result from a channeled asthenospheric flow that could link the Réunion Plume and the Central Indian Ridge. The Rodrigues Ridge basaltic structure was formed between 8 Ma and 10 Ma (Dyment et al., 2007) and has a plume geochemical signature (Mahoney, Natland, White, Poreda, Bloomer, Fisher, et al., 1989). It is elongated in the west-east direction and connects the transform fault from Mascarene Plateau to the Central Indian Ridge (CIR).

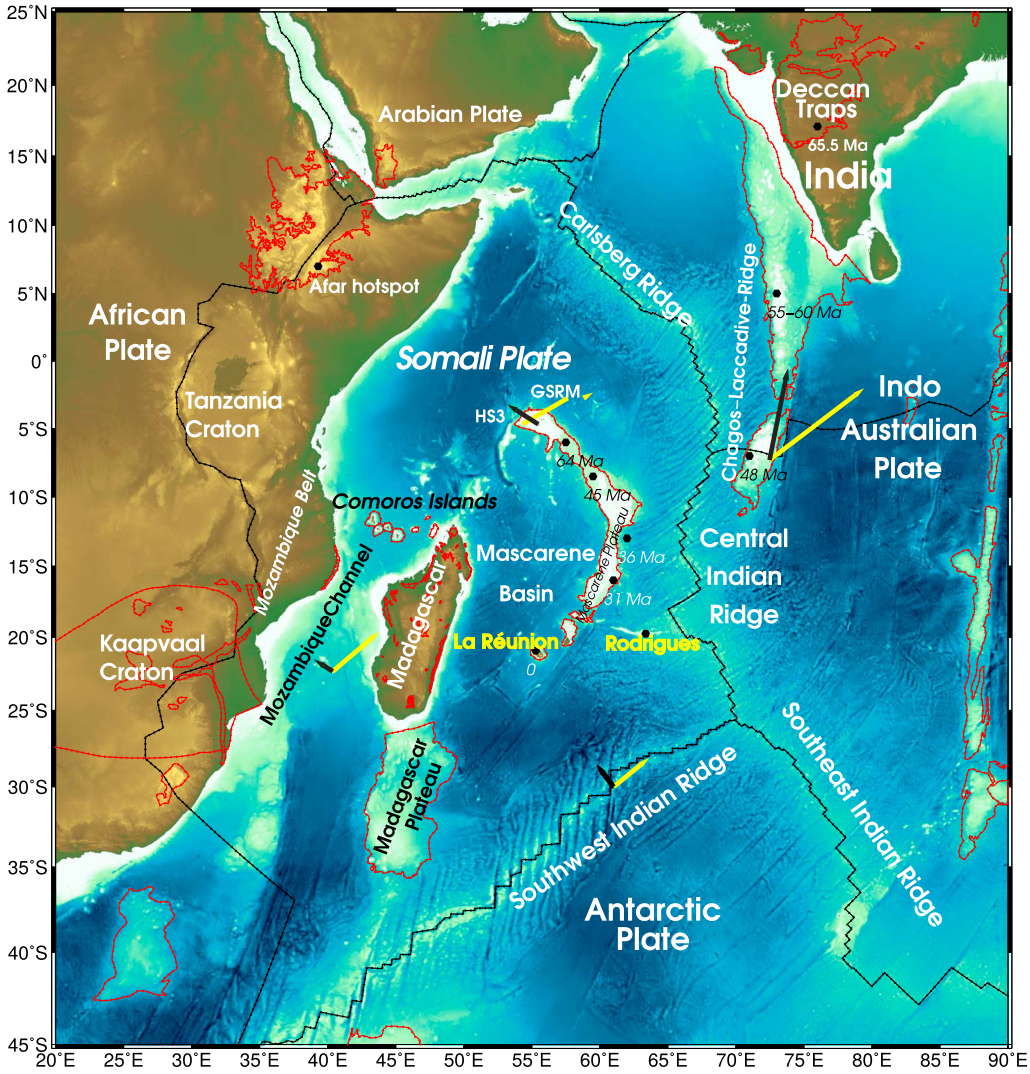

Figure 1. Bathymetry and topography map of the study area (ETOPO1) (Amante & Eakins, 2009). Absolute plate motion vectors (1 cm/yr) calculated from the no net rotation global strain rate model (Kreemer, 2009) are shown in yellow and from the HS3-Nuvel1A model (hot spot frame) (Gripp & Gordon, 2002) in black. The domains inside the red lines represent the volcanic provinces. Crustal ages (Duncan et al., 1990; Duncan & Hargraves, 1990) are indicated with black or white circles.

Another example of the complexity of the region is the controversial interpretation of Comoros Archipelago, which is located in the northern Mozambique Channel between the northern tip of Madagascar and Mozambique. The development of the Comoros Islands might be interpreted as a result of lithospheric deformation in the general context of the East African Rift (Michon, 2016), rather than the surface expression of a deep mantle plume, as was initially proposed (Nougier et al., 1986; Upton, 1980).

Due to the complexity of this area, several studies have proposed alternative models for the geological evolution of the Indian Ocean and the Réunion plume, which have disconnected Deccan Traps and Laccadives-Maldives-Chagos Ridge from La Réunion plume. Burke (1996) proposed a younger plume for the buildup of Mauritius, Rodrigues Ridge, Rodrigues Island, and La Réunion Island. This was different from the old plume that was extinct about 30 Ma, which might have been responsible for the old part of the track on the Indian Plate. Sheth (1999) proposed that the Deccan volcanic episode was the result of a protracted process of lithospheric rifting. Then the successive Chagos-Laccadive Ridge and the entire seamount chain from there up to La Réunion Island would be a southerly propagating fracture zone.

From a seismological point of view, both global (Burgos et al., 2014; Debayle & Ricard, 2012; French & Romanowicz, 2015) and regional (Debayle & Lévêque, 1997; Lévèque et al., 1998; Montagner, 1986b; Montagner & Jobert, 1988) studies performed with different data sets and methodologies have suffered from the paucity of seismic stations in this area. These models had lateral resolution of 1,000 km or more, which was too low to investigate possible interactions between the plume and the CIR, or the influence of the flow of the plume material on the lithosphere and asthenosphere.

We aimed to improve the resolution of the velocity structures around La Réunion Island by incorporation of a large data set provided by the Réunion Hotspot and Upper Mantle-*Réunions Unterer Mantel* (RHUM-RUM) experiment (Barruol & Sigloch, 2013). Here section 2 introduces the data set used and the preprocessing of the data. Section 3 describes the phase/group measurements and their regionalization. Section 4 details the successful adoption of a transdimensional inversion scheme to generate a model of anisotropic shear velocity variations. Sections 5 and 6 present the model in the western Indian Ocean and discuss the Réunion plume interaction with the ridge and with the large deep anomaly beneath the entire Mascarene Basin. The supporting information provides the resolution tests, the comparisons with global models, and more details on the inversion procedure.

2. Data

This study is based on the use of data from the RHUM-RUM (Réunion Hotspot and Upper Mantle-Réunion's Unterer Mantel, code YV) project (Barruol & Sigloch, 2013), which consisted of the deployment of 57 broadband ocean bottom seismometers (OBS) positioned on the ocean floor for 13 months (October 2012 to November 2013) over an area of $2{,}000 \times 2{,}000\ km^2$ surrounding Réunion Island. A further 37 temporary broadband land stations were deployed on Madagascar and on the Comoros and Eparses Islands in Mozambique Channel, for 2 to 3 years (Barruol & Sigloch, 2013). Two different types of OBS stations were deployed: 48 German wideband *Deutscher Geräte-Pool für Amphibische Seismologie* (DEPAS) stations and 9 French broadband stations from the *Institut National des Sciences de l'Univers* (INSU). Of these 48 DEPAS OBS, 39 were equipped with a Güralp CMG-40T three-component seismometer with a corner period of 60 s. The remaining nine German instruments were equipped with a seismometer prototype with a corner period of 120 s, but all of them failed recording data under the deep-sea conditions. The nine INSU stations were equipped with Trillium-240 seismometers with a corner period of 240 s. For a more detailed description of the RHUM-RUM OBS stations performances, the reader is referred to Stähler et al. (2016).

The data set also includes data from 33 temporary broadband land stations in Madagascar and East Africa, from the U.S. Madagascar, Comoros, Mozambique (MACOMO) project (Pratt et al., 2017; Wysession et al., 2012). Permanent stations from the International Federation of Digital seismograph Networks (FDSN; i.e., GEOSCOPE, GEOFON, and IRIS/USGS) inside and around the western Indian Ocean, were also used. The starting data set was formed by events with magnitudes (M_w) $\geq$ 5.5 and epicentral distances between 30° and 120°, which were collected using ObspyDMT (Hosseini, 2015). The data were manually selected for high signal-to-noise ratio. The final data set consisted of 15,000 Rayleigh wave seismograms that corresponded to the vertical component of the long-period channel. The geographical distributions of sources and receivers are shown in Figure 2. Due to the important seismic activity that originated in Indonesia, Japan, and the western Pacific, most of the seismic raypaths came from a northeastern direction. Therefore, other complementary events were added to increase the azimuthal coverage along the other directions, in particular, from the west and southwest. Figure 3 shows traces recorded by land and OBS stations.

3. Methods

The first step in this tomography procedure is the measurement of the phase and group velocities for the Rayleigh wave fundamental modes, along each selected great circle path. The fundamental mode dispersion curves were measured in a broad period range for the group (16–200 s) and phase (36–250 s) velocities. The group velocity measurements are extended down to a low period (i.e., 16 s) to provide better constraint on the crustal structures. The long-period measurements for the phase velocity (i.e., 250 s) allow the imaging of the deeper parts of the upper mantle. Finally, ~9,000 paths were selected for the group velocity measurements and $\sim 8,000$ paths for the phase velocity measurements.

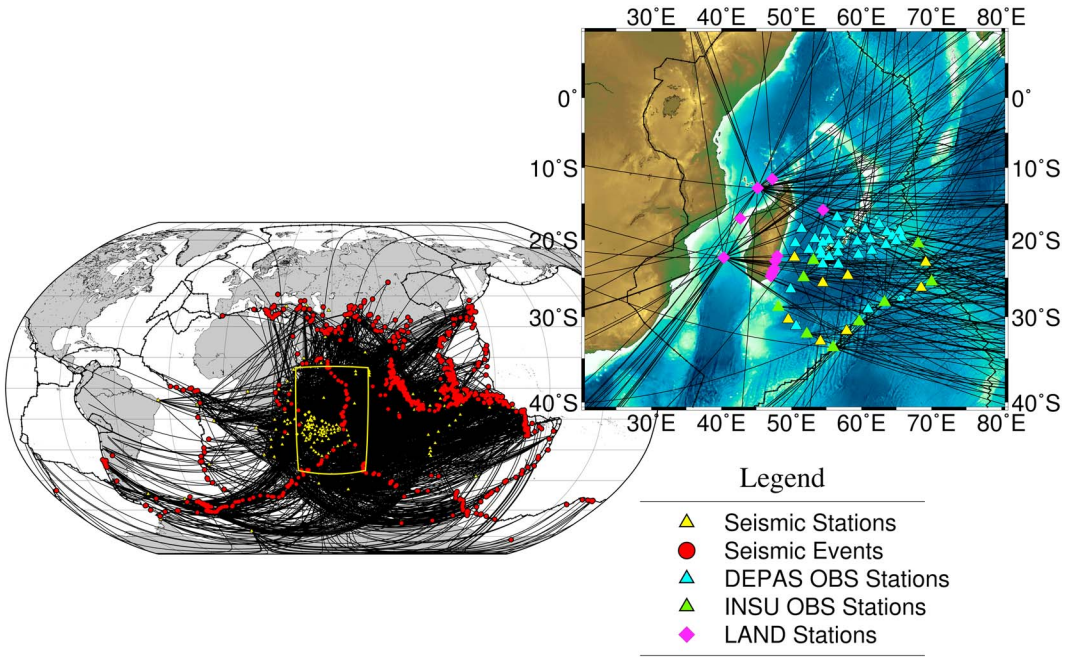

Figure 2. Global distribution of the ~300 earthquakes sources (red) and 130 stations (yellow) used in this study. Black lines show the great circle paths. The magnified panel (right) shows the distribution of the RHUM-RUM stations and the final raypath coverage used in the procedure.

3.1. Phase Velocity Measurements

The mean phase velocity between the source and receiver is extracted using the "roller coaster" waveform inversion technique for surface waves (Beucler et al., 2003; Stutzmann & Montagner, 1993). We consider here only the time window of the fundamental mode of the Rayleigh waves, even though the method makes it possible to also extract higher mode phase velocities. In the Fourier domain, the forward problem for fundamental mode can be written as follows (Kanamori & Given, 1981):

$$A^R(\omega)\exp(i\Phi^R(\omega)) = A_0^S(\omega)\exp\left\{i\left[\Phi_0^S(\omega) + \omega\Delta\mathbf{n_s}\left(1+\frac{\delta\mathbf{n}}{\mathbf{n_s}}\right)\right]\right\}, \quad (1)$$

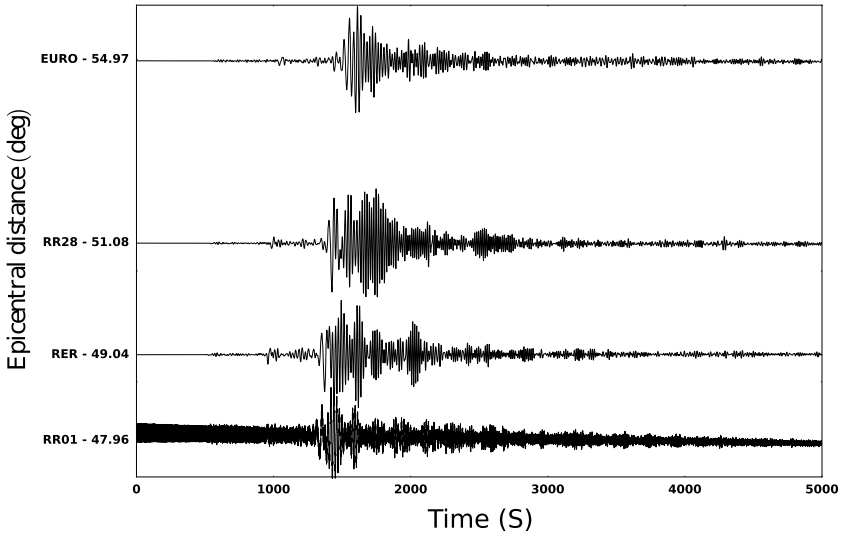

Figure 3. Seismograms corresponding to the event that occurred in Pakistan $M = 7.7$ (24 September 2013) that were recorded by the French INSU OBS RR28 station, the German DEPAS OBS RR01 station, the Geoscope RER land station (La Réunion Island), and the temporary EURO land station deployed on Europa island in Mozambique Channel.

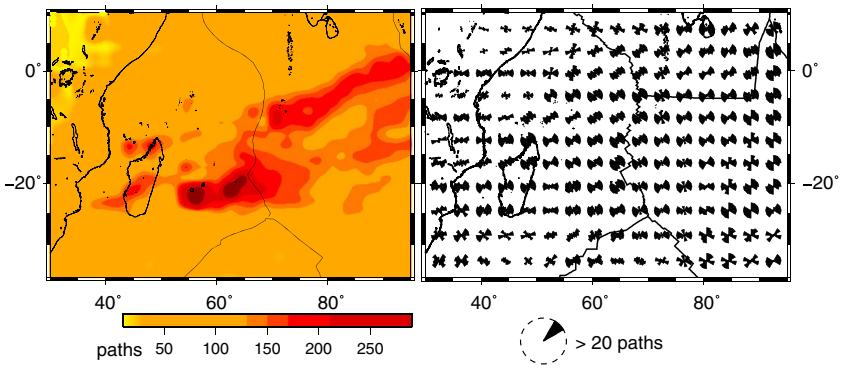

Figure 4. Data set used in the phase velocity calculation. (left) Density path map. (right) Azimuthal coverage of the area, where the number of paths per unit area (2° × 2° cell) is binned in the azimuth range of 30°, and the vectors are saturated at 20 paths. However, the density path beneath Réunion and the central/eastern part of the map is higher than beneath Africa. The path coverage is redundant everywhere.

where ω is the angular frequency, A_0^R and Φ_0^R are the amplitude and phase, respectively, for a recorded seismogram spectrum, Δ is the epicentral distance in kilometers, and $\mathbf{n_s}$ is the slowness at frequency ω computed for a reference model. A_0^S and Φ_0^S are amplitude and phase terms, respectively, that include source, geometrical spreading, seismic attenuation, and receiver response terms. The phase shift due to the propagation in a real medium resides in the term $\exp[i\omega\Delta\delta\mathbf{n}]$, the slowness perturbation.

The inversion scheme uses least squares optimization (Tarantola & Valette, 1982) to find the best slowness values as a function of the frequency around the reference model, starting from those at the long period (long-wavelength variations) and using these as a constraint to refine the inversion at the short period (short wavelength). To estimate the a posteriori reliability of the phase velocity calculations, synthetic seismograms are reconstructed using the inverted phase velocity, and correlations between real and synthetic data are used to select accurate measurements. Signals that do not show good correlation with respect to the real seismograms are rejected. At this stage, almost 8,000 seismograms were selected from more than 14,000 seismograms. Figure 4 shows the path density map and the azimuthal coverage of the area for the phase velocity.

The final error for the phase velocity measurement is approximated by $\sigma_d = C_j^S(\mathbf{r},\omega)\cdot 0.005$, where C_j^S is the measured phase velocity. To illustrate the procedure, Figure 5 (left column) shows three examples of waveforms filtered in the (33–333 s) period band. The corresponding phase velocity curves are shown on the right. The trace shown in Figure 5a was recorded by the Geoscope land station (RER) located on La Réunion Island. Figures 5b and 5c show the vertical component records for the two OBS stations RR40 (broadband) and RR01 (wideband). The traces recorded the 11 November 2012 earthquake that occurred in Thailand ($M = 6.8$). The waveforms are recovered very well for all three of these stations. The differences in the period ranges of the phase velocity calculations are caused by the different sensitivities of the sensors of the DEPAS and INSU stations. Moreover, the different design of the RR01 station framework induces a higher signal-to-noise ratio, which influences the phase velocity results, and consequently the waveform retrieval, as shown in the dispersion curves in Figure 5 (right column). For a more detailed description of the RHUM-RUM OBS stations performances, the reader is referred to Stähler et al. (2016) and Scholz et al. (2017).

3.2. Group Velocity Measurements

The mean group velocity for each source-receiver path was measured for the Rayleigh wave fundamental mode using time-frequency analysis (Levshin, 1985). This method uses a system of narrowband Gaussian filters with varying central frequency that do not introduce phase distortion, and it provides good resolution in the time-frequency domain. The group velocity calculation is performed in the period range of 16 s to 200 s. A strict quality check criterion is applied when the automatic picking of the dispersion curves resulted in complex waveform phenomena due to scattering, multipathing, and interfering overtones. To remove bad measurements, only the frequency range where the group velocity appeared well defined was picked out visually. Figure 6 shows the group velocity dispersion curves with the manual picks for the same stations (i.e., RER, RR40, and RR01) and the same event as in Figure 5. Figure 7 shows the azimuthal coverage and path density coverage relative to the final group velocity data set.

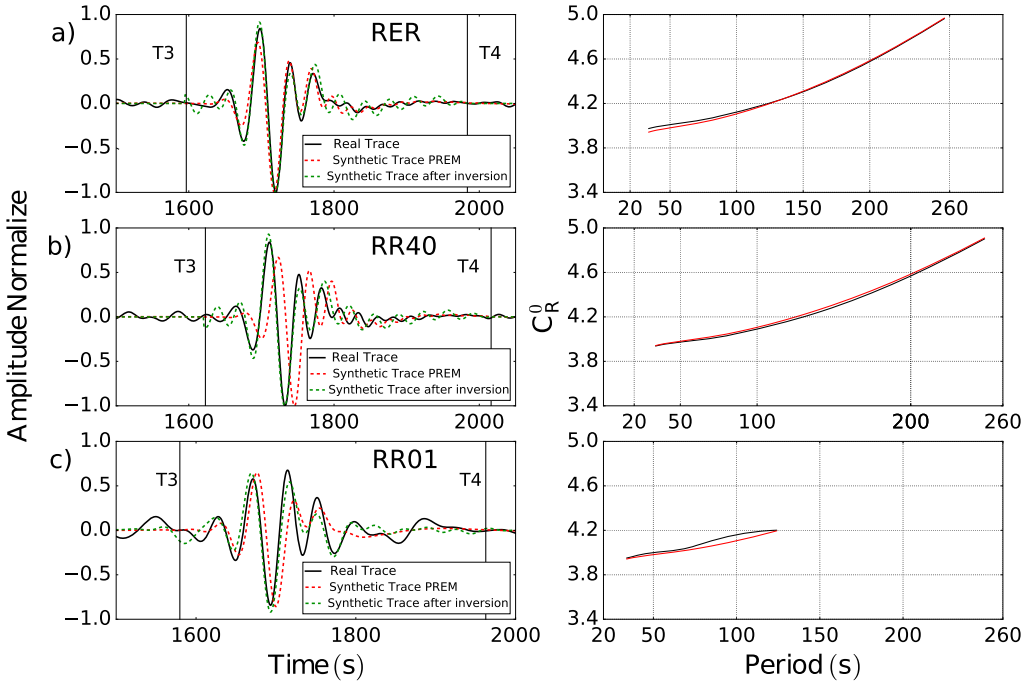

Figure 5. Quality of the fundamental mode measurements is assessed in windows delimited by T3 ($\Delta/U_{\max_0}$, where Δ is the epicentral distance, $U_{\max_0} = 4.0$ km/s maximum velocity of the fundamental mode) and T4 ($\Delta/U_{\min_0}$, where $U_{\min_0} = 2.8$ km/s minimum velocity of the fundamental mode). (left column) Recorded traces for an earthquake in Thailand $M = 6.8$ for stations (a) RER, (b) RR40, and (c) RR01. The data are in black (filtered in the (33–333 s) period band), the synthetic before and after the inversions are in red and green, respectively. (right column) Measured fundamental mode phase velocity (black), compared to the predicted ones for the Prem model (red).

3.3. Regionalization

Phase and group velocity lateral variations are computed using the regionalization method (Montagner, 1986a), as improved by Debayle and Sambridge (2004). The Earth can be considered as a medium where seismic parameters vary smoothly and velocity gradients are not strong (Woodhouse, 1974). In the framework of geometrical ray theory approximation, the relationship between mean phase/group velocities for a given path, $V_{R_s}(\omega)$, and local phase/group velocities at position M can be written as follows:

$$\frac{\Delta}{V_{R_s}(\omega)} = \int_S^R \frac{1}{V(\omega, M)} \mathrm{d}s, \tag{2}$$

where Δ is the epicentral distance between source S and receiver R.

The analysis of the local velocity is based on the Rayleigh principle combined with the harmonic tensor decomposition of Backus (1970). Smith and Dahlen (1973) have shown that for a slight anisotropic Earth, the local azimuthally varying velocity $V(\omega, M, \Psi)$ is expressed at location M for the angular frequency ω and azimuth Ψ, as follows:

$$\begin{aligned} V(\omega, M, \psi) &= V_{\mathrm{REF}}(\omega) + a_0(\omega, M) \\ &+ a_1(\omega, M)\cos 2\psi + a_2(\omega, M)\sin 2\psi \\ &+ a_3(\omega, M)\cos 4\psi + a_4(\omega, M)\sin 4\psi, \end{aligned} \tag{3}$$

where ψ is the azimuth of the considered direction, a_0 and a_i ($i = 1$–4) are the isotropic terms (mean from all of the azimuths) and the coefficients of azimuthal anisotropy, respectively, and V_{REF} is taken as the mean of the measured velocities at frequency ω.

Montagner and Nataf (1986) demonstrated that Rayleigh waves are mainly sensitive to 2Ψ coefficients. Therefore, we considered only these terms in the procedure. To regularize the inversion, it is necessary to

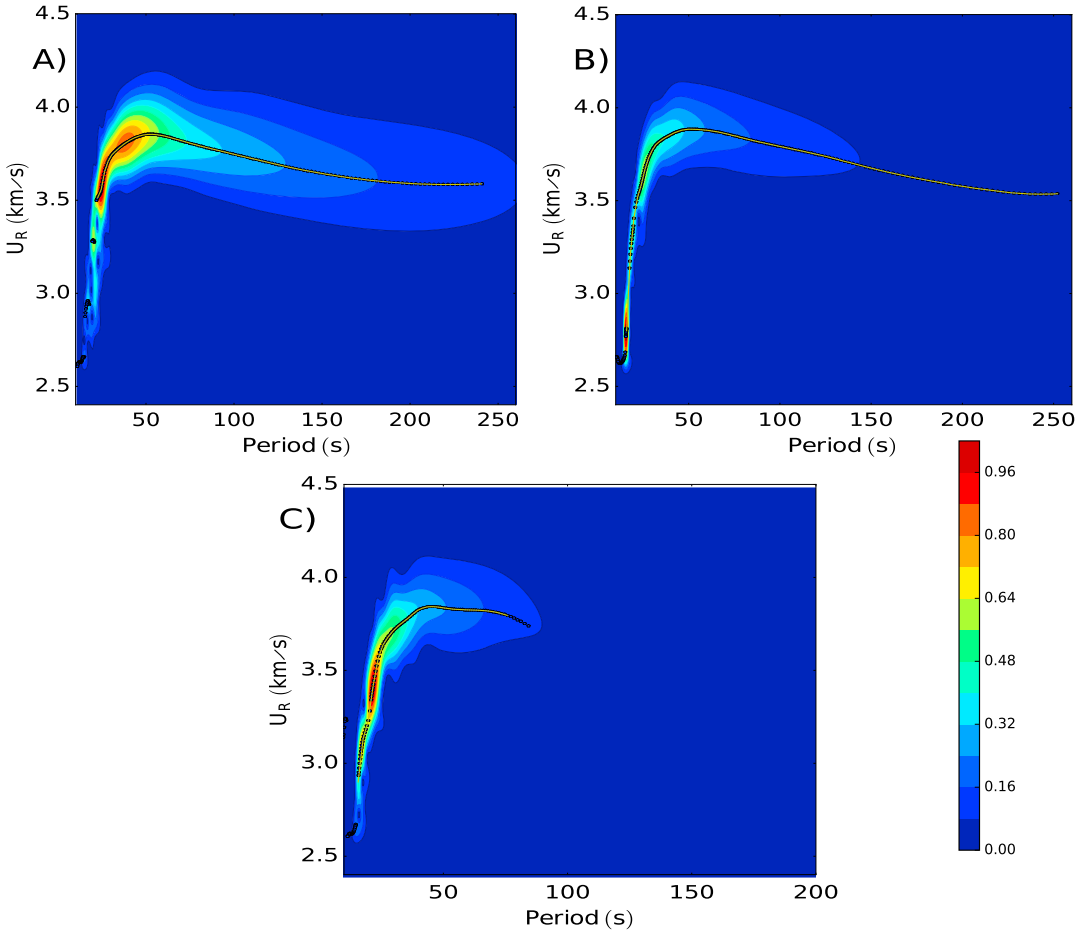

Figure 6. Dispersion curves for an earthquake in Thailand $M = 6.8$ 11 November 2012, as recorded by (a) RER, (b) RR40, and (c) RR01. The colored backgrounds indicate the time frequency signal amplitudes, with red-based colors as the largest amplitudes. The yellow lines show the manually picked dispersion curves. The measured period range is broader for RER and RR40 than for RR01 due to the different sensors in the stations.

introduce some a priori constraints. This can be done through the definition of an a priori model m_0 and an a priori covariance function $C_{m0}(M, M')$ (Montagner & Nataf, 1986).

$$C_{m0}(M, M') = \sigma_m(M)\sigma_m(M')\exp\left(\frac{-\Delta^2_{M,M'}}{2L^2_{\text{corr}}}\right), \tag{4}$$

where M and M' are two geographical points that are separated by a distance Δ. The exponential term defines a Gaussian function with a standard deviation given by a correlation length L_{corr}. The least squares inversion is controlled by two parameters: the a priori error on the parameters and the correlation length. The a priori error on the parameters corresponds to the uncertainties on the velocities and anisotropy and defines the variation range of the model parameters. The correlation length L_{corr} acts as a lateral spatial filter that imposes correlations between points separated by distances of the order L_{corr} and affects the amplitude and the lateral variations of the results. In this study, we use the code developed by Debayle and Sambridge (2004), which is based on the same technique as Montagner and Nataf (1986), but use a more efficient Earth model parametrization based on Voronoi cells and apply an optimization strategy that enables very large data sets to be handled. The code regionalizes the average phase/group velocity of the paths on the entire Earth. The regionalized model is given on a grid of $1° \times 1°$, keeping where there are no paths the reference velocity (V_{REF}) and, where there are isolated paths (with no crossing paths), the residual is distributed along the path. Several tests were performed using different sets of input parameters (correlation lengths, L_{corr}, a priori errors on velocities, σ_i, and anisotropy σ_a) to study the influence of these on the inversion results and on the final values of the variance reduction and the χ^2 criteria.

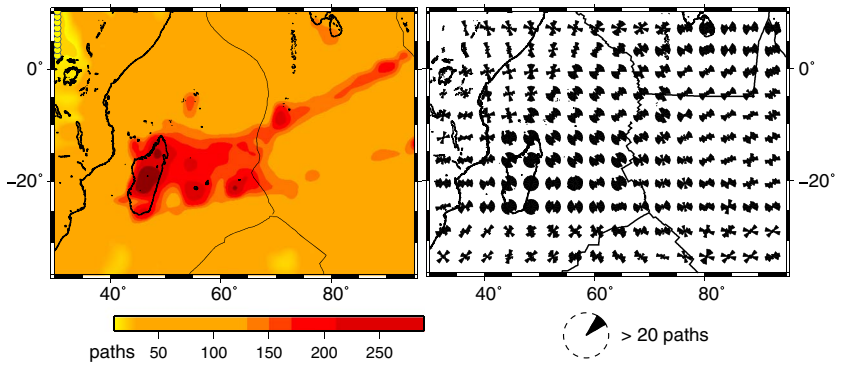

Figure 7. Data set used in the group velocity calculation. (left) Density path map. (right) Azimuthal coverage of the area, where the number of paths per unit area (2° × 2° cell) are binned in the azimuth range of 30°, and the vectors are saturated at 20 paths. There is higher density of paths beneath Réunion and the central/eastern part of the map than beneath Africa; the path coverage is redundant everywhere.

In this procedure, good compromise between resolution, variance reduction, and χ^2 criteria corresponds to a correlation length of 200 km, an a priori model error for the isotropic parameters, $\sigma_i = 0.05$ km/s, and for the anisotropy parameters, $\sigma_a = 0.03$ km/s. These tests show that the location of the main velocity anomalies remains substantially unchanged in all of the inversions. Finally, we checked that the inversion results are not biased by preferential orientation of some paths in the NE-SW direction. The same inversion was performed with a sub−data set that consisted of a more homogeneous azimuthal path coverage, with similar results obtained as with the entire data set. Errors on regionalized velocities are computed using a bootstrapping approach (Efron & Tibshirani, 1991), which provides the standard deviation of 20 random samplings of 80% of the whole data set. The reliability of the velocity regionalization was also estimated with checkerboard synthetic tests (supporting information Text S1.1). We recovered 500 km wide lateral structures with good lateral resolution, especially for the central zone of the area (supporting information Text S1.1 and Figures S1−S4).

4. Inversion Versus Depth of Dispersion Data Set

The inversion was performed independently for each location for a 1° grid in latitude (θ) and longitude (Φ). The code developed by Haned et al. (2016) was used, which follows a transdimensional inversion scheme, where the data themselves constrain the maximum allowable complexity in the model, rather than specifying this beforehand.

The *Sv* wave velocity model, V_{sv}, is expanded in terms of a variable number of B splines that have unknown positions and coefficients. This can be written as follows:

$$V_S(z) = V_S^0(z) + \sum_{m=0}^{M-1} W_m N_{m,2}(z), \tag{5}$$

where $N_{m,2}(z)$ is the mth nonuniform quadratic B spline basis function (De Boor, 1978) that describes the model, M is the number of B spline basis functions, W_m is the weighting coefficient, and $V_S^0(z)$ is the a priori reference *S* wave velocity at each location (θ, Φ). $V_S^0(z)$ is a combination of a modified version of crust1.0 (Laske et al., 2013), and PREM (Dziewonski & Anderson, 1981), where the discontinuity at 220 km is replaced by a gradient. The construction of the a priori crustal model is discussed in supporting information Text S2.

This transdimensional inversion consists of two nested loops: for a given spline basis, the inner loop uses the simulated annealing optimization algorithm to calculate the optimum model weighting coefficients, W_m, by minimizing the data misfit function (χ_d^2) between the measured and modeled phase/group velocities. The outer loop is used to find the optimum spline basis (number of splines M and their shape). For a given number of splines M, the shape of the M splines can vary continuously from being concentrated toward the shallow layers,to being more uniformly distributed over the depth range of interest. The outer loop selects the optimum spline basis by minimizing a cost function defined as the mean of the χ_d^2 value attained in the inner loop

and the norm of a posterior model covariance matrix. The golden section search method (Press et al., 1992, chap. 10.1.) is used to minimize this cost function. The dimension of the *Sv* wave velocity model (i.e., the number of splines and their shape) is obtained by finding a compromise between the level of the data fit and the norm of the model a posteriori covariance matrix. This compromise corresponds to the well-known trade-off between model resolution and variance. The transdimensional inversion controls the model complexity to avoid data overfitting. For example, if for a given location (latitude and longitude) the data (phase/group velocity) errors are large, the outer loop minimization routine reduces the dimension of the model (number of splines) automatically. The model complexity reduces as the data variance becomes larger. We checked with synthetic tests that the *Sv* wave velocity model and the corresponding number of splines are accurately retrieved by the inversion (see supporting information Text S1.2 and Figure S5). This method differs from the transdimensional Bayesian inference as defined by Sambridge et al. (2013), as we do not use an a posteriori probability density function to estimate the model and instead keep a single optimal model that achieves the minimum cost function.

The inversion procedure described above is used to retrieve the anisotropic *S* wave velocity model as follows. The azimuthally anisotropic *S* wave velocity model, V_{sv}, at given depth *z* can be written as a first-order approximation as follows (Montagner & Nataf, 1986):

$$V_{sv}(\psi) = \sqrt{\frac{L + G_c \cos 2\psi + G_s \sin 2\psi}{\rho}}, \tag{6}$$

where ψ is the azimuth, ρ is the density, and L, G_c, and G_s are the anisotropy parameters. We use the isotropic forward modeling code of Saito (1988) for computing the phase and group velocities for a given Earth model. To retrieve the anisotropic parameters, four azimuths were considered, $\Psi_i = 0, \pi/4, \pi/2, \text{and} 3\pi/4$, and for each of these the isotropic inversion is performed using the transdimensional inversion method, to obtain the corresponding $V_{sv}(\psi)$ velocity model. We can then resolve the linear system of equation (6) to obtain the parameters L, G_c, and G_s as a function of depth.

To take into account that seismic wavelengths are different at periods from 16 s to 250 s, the tomographic model is obtained in two steps. First a low-resolution azimuthally anisotropic *S* wave velocity model is determined from the phase and group velocities (period range, 16–250 s) regionalized with a correlation length of 800 km, using the procedure described above. We then use the isotropic part of this low-resolution model as a starting model and follow the same procedure to invert the phase and group velocities, regionalized with a shorter correlation length of 200 km. The final errors on the *Vs* parameters are estimated using the diagonal terms of the covariance matrix evaluated, following Tarantola and Valette (1982). Synthetic tests on the one-dimensional inversion method are provided in the supporting information (Figures S5 and S6).

5. Tomographic Model

The S_V wave velocity model is presented in Figure 8 for the depths of 50, 100, 150, and 200 km. At shallow depths (i.e., 50 km), the model retrieves a classic correlation between a velocity anomaly and the surface tectonic structures, such as mid-oceanic ridges, old seafloor basins, and the continental lithosphere.

Mid-ocean ridges are characterized by slow velocity signatures between 30 km and 100 km in depth (Figure 8). At 50 km in depth, the slow velocity amplitude is weaker under the Southwest Indian Ridge (SWIR) than under the Southeast Indian Ridge and the Central Indian Ridge (CIR). The strongest high velocities in the depth range of 20 km to 180 km correspond to the continental lithosphere in Madagascar and eastern Africa and to the old seafloor basins (Mascarene Basin, 90 Ma and Mozambique Channel, 150 Ma). The positive anomaly amplitude in the ocean basins increases smoothly with the age and thickness of the lithosphere, from +1% for the younger and thinner (20 km) lithosphere close to the ridges, up to +6% for the old and thick seafloor in the Mascarene (80 km) and Mozambique (100 km) Basins. The intensity of the positive signature of Madagascar (∼+4%) decreases with depth and disappears around 160 km in depth.

Between 50 km and 100 km in depth, a slow velocity anomaly connects the Réunion hot spot and the CIR, under the Rodrigues Ridge at a latitude of 18° to 20°S (Figure 8). At greater depths (i.e., 150–200 km), a large and strong slow velocity anomaly is observed from the Mascarene Basin at the north to La Réunion Island at the south, which is elongated along a northeast direction toward the CIR.

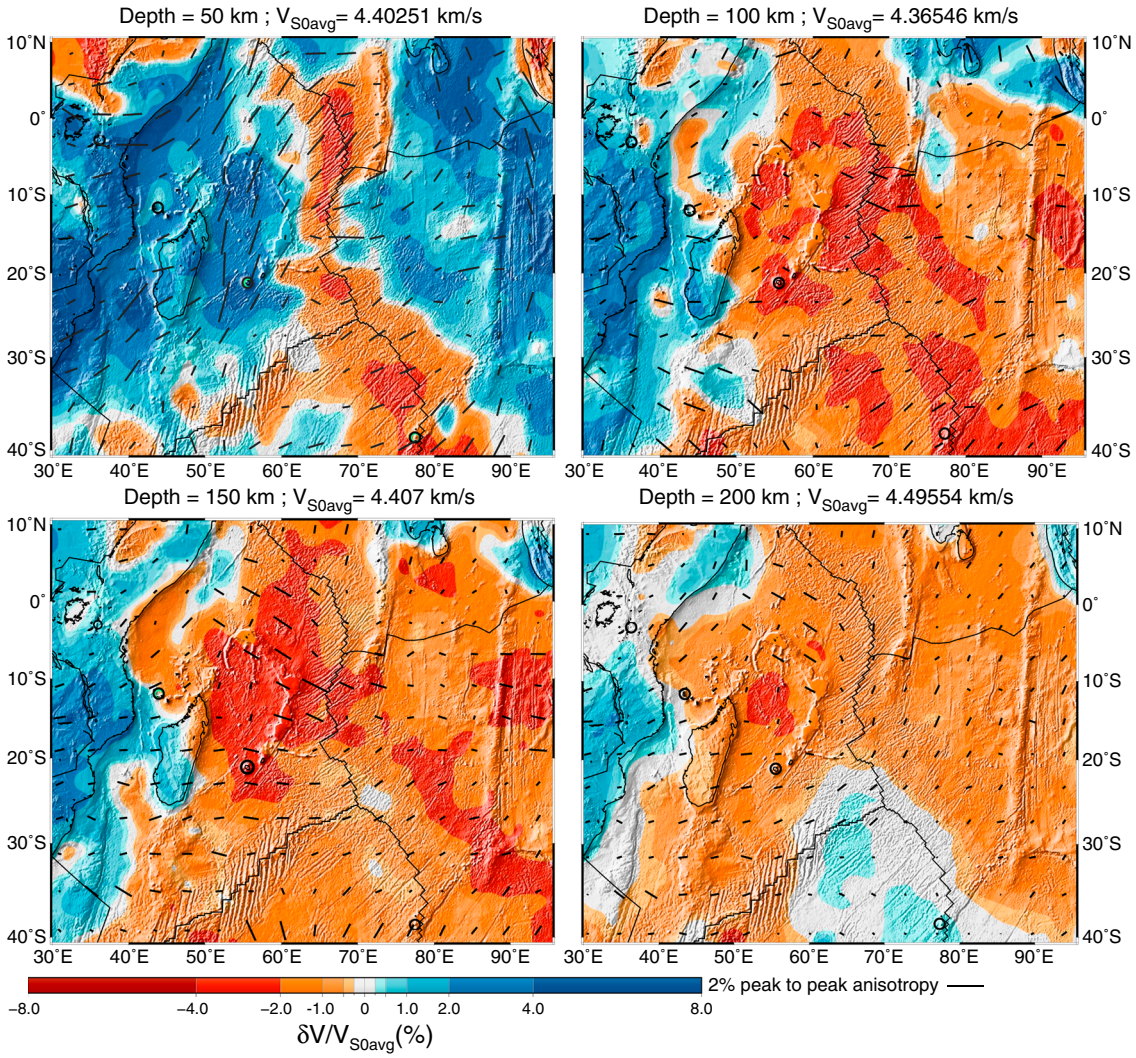

Figure 8. S_V wave velocity perturbation with respect to the mean velocity at the different depths of 50, 100, 150, and 200 km. Fast anisotropy directions are plotted with bars, where the strength is normalized with respect to the maximum value at each depth. Black circles indicate the hot spot locations in the area.

The bars in Figure 8 indicate the amplitude and direction of the azimuthal anisotropy. The presence of plumes and ridges in this region makes the pattern of azimuthal anisotropy particularly challenging. However, in some zones at the edge of the studied area (i.e., eastern Africa, south of the southwest Indian Ocean, and the Antarctic Plate; Figures 4–7), fewer paths were collected, and most of these showed the same directions. This data set resolves the azimuthal anisotropy direction well everywhere else.

These results clearly show that the anisotropy is concentrated between 50 km and 150 km in depth and starts to disappear at 200 km in depth. This suggests that most of the upper mantle deformation is concentrated within the lithosphere and the asthenosphere. At 50 km in depth, the fast azimuthal anisotropy direction close to the CIR follows the direction of the spreading. This is not the case for the SWIR, where the azimuthal anisotropy is oriented parallel to the SWIR. In the old ocean basins, such as Mascarene, Mozambique, and Chagos, the azimuthal anisotropy maintains the general northeast-southwest direction parallel to the no net rotation absolute plate motion calculated from the global strain rate model (Kreemer, 2009).

At asthenospheric depths (i.e., >100 km), the azimuthal anisotropy direction is west-east in the West Indian Ocean, Madagascar, and Comoros. North of the Seychelles Islands, the fast velocity direction rotates from the north-south direction at 50 km to 100 km in depth to the northwest-southeast direction at 150 km in depth,

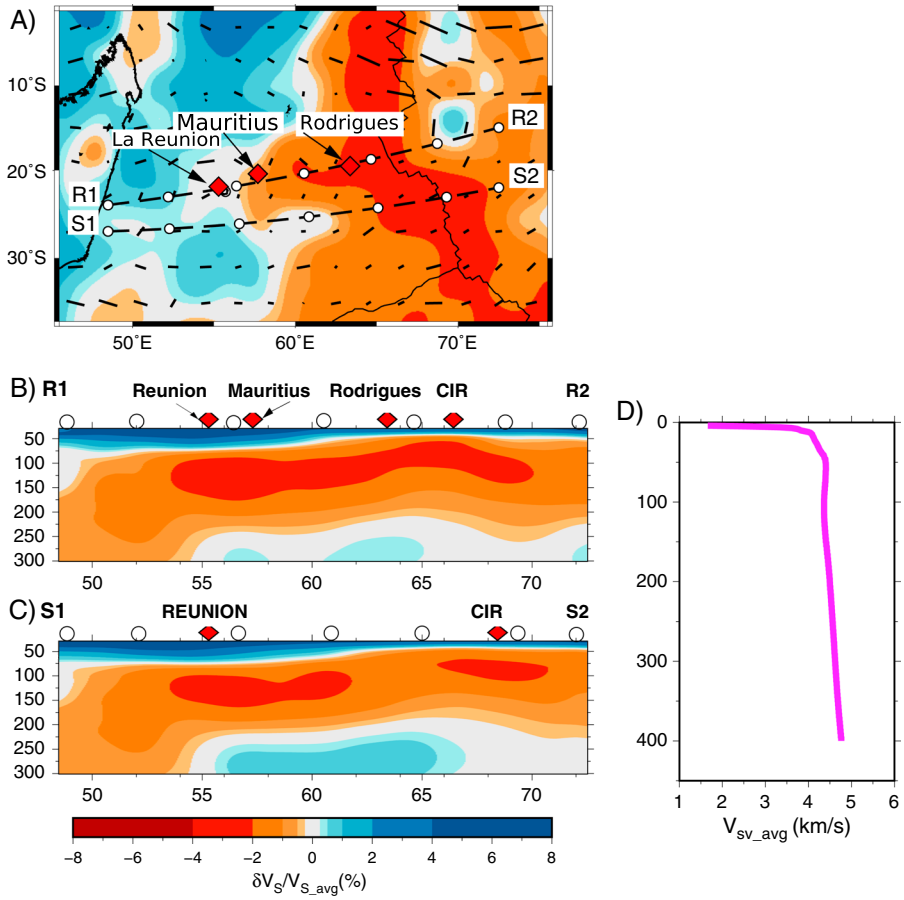

Figure 9. (a) Map of the *S* wave velocity model at 80 km in depth. Réunion and Rodrigues Islands are indicated by red diamonds, and the dotted lines show the location of the cross section. (b, c) Cross sections showing the development and intensity of the channeled flow in the area of Réunion-CIR. The sections are plotted as a function of depth and latitude. (d) Average *S* wave velocity as a function of depth. Velocity anomalies plotted in Figures 9a–9c are determined with respect to this average model.

in agreement with the absolute plate motion from the HS3-Nuvel1A model (hot spot framework) (Gripp & Gordon, 2002) with decreasing amplitude. At 200 km in depth, the azimuthal anisotropy amplitude decreases significantly while preserving the same fast direction of the overlying depths.

The model was compared with three global models: 3D2015 (Debayle et al., 2016), BM12UM (Bassin et al., 2000; Burgos et al., 2014), and SL2013sv (Schaeffer & Lebedev, 2013). The correlation between the isotropic component of the *S* wave velocity in the present model and these three published models is between 0.65 and 0.80. Anisotropic fast direction differences between the present and these global models are less than 30° in 60% of the model. Comparisons between models with maps and cross sections are included in supporting information Text S3. There is general good agreement between the models, although the features described in the next section are new and/or better resolved by the present model due to the denser station coverage in the area of interest.

6. Discussion

6.1. The Channel Between La Réunion and the Central Indian Ridge

The tomography model at 80 km in depth shows a strong and continuous slow velocity anomaly (−5%, −4%) from Réunion Island toward the CIR (Figure 9a). It has a thickness of ~200 km, which is constant, although it is progressively shallower toward the CIR (Figure 9b).

At shallower depths, the fast velocity anomaly associated with the lithosphere is visible down to 75 km beneath La Réunion Island, and it is progressively shallower toward the CIR; fast anomalies are observed down to 47 km beneath Mauritius and down to 30 km beneath Rodrigues. The lithosphere thickness variation is

in agreement with the thicknesses obtained from a receiver function study by Fontaine et al. (2015), who reported thicknesses of 70 km beneath Réunion, 50 km beneath Mauritius, and 33 km beneath Rodrigues. The thinning of the lithosphere toward the CIR can be explained by age-progressive lithospheric cooling and thickening and also by thermochemical erosion due to heat conduction, as proposed by numerical modeling (Thoraval et al., 2006). Figure 9c shows that the connection between the hot spot and the CIR loses intensity south of La Réunion Island (longitude, 55°E). These results suggest a connection with lateral transport of solid plume material from Réunion to the ridge through an asthenospheric channel along Rodrigues Ridge (latitude, 19°S). Such an asthenospheric channel was proposed by Morgan (1978), Sleep et al. (2002), and Yamamoto et al. (2007a, 2007b) but has never been mapped to date. This channel flow can also explain some other observations that characterize Rodrigues Ridge and the Rodrigues Island area, such as a thicker oceanic crust, shallow and smooth bathymetry, and chemically enriched mid-ocean ridge basalts (Dyment et al., 2007; Hofmann, 1997; Mahoney, Natland, White, Poreda, Bloomer, & Baxter, 1989; Schilling, 1973), which are direct results of erupting magmas on the surface and intruding magmas at lithospheric depth. East of the Rodrigues Ridge, the segment of the Central Indian Ridge located between Egeria and Marie Celeste fault zones, is also significantly shifted toward the west, in the direction of the Réunion and Mauritius Islands, with respect to the other ridge segments. All of these observations support the hypothesis of an off-axis plume-ridge interaction between the upwelling hot material in Réunion and the CIR. The asthenospheric connection between the Réunion hot spot and the CIR is also supported by the azimuthal anisotropy results here, as illustrated in the maps of Figure 9a. The values of the azimuthal anisotropy in this area are small (<1%), and this might indicate a vertical small-scale upwelling: the fast direction pattern shows a NW-SE direction north of La Réunion Island and a NE-SW direction south of Réunion Island, which creates a convergent east-west flow at a latitude of 18° to 20° toward the CIR. The direction of the fast axes of the observed azimuthal anisotropy beneath Réunion, Mauritius, and Rodrigues Islands (where the permanent stations are located) is compatible with results from *SKS* splitting analysis (Barruol & Fontaine, 2013; Scholz et al., 2016) and in agreement with independent geodynamic models (Bredow et al., 2017).

6.2. Large Slow Anomaly Beneath Mascarene Basin

At shallow depths (Figure 8), the Mascarene Basin shows a compact and thick oceanic lithosphere with a high-velocity anomaly between +2% and +7%. At 130 km to 200 km in depth an asymmetric distribution of slow velocity signatures can be observed, with respect to the CIR in the western part of the Indian Ocean. Our model shows a wide slow velocity anomaly beneath the entire Mascarene Basin between Madagascar, Réunion, and the Seychelles in the west part of Indian Ocean. At 150 km in depth, the slow anomaly is elongated toward the northeast direction from Réunion up to the northern part of the CIR, with an amplitude from −3% to −6%. At 200 km in depth, the strongest slow anomaly is centered north of Réunion Island, beneath the old Mascarene oceanic lithosphere.

Cross section A1–A2 of Figure 10 show this large slow velocity anomaly at depth in the northern part of Mascarene Basin. Cross sections C1–C2 and D1–D2 show how the slow velocity signature reaches the surface to the east toward the CIR along the Seychelles Arc and develops at depth beneath Africa to the west. The northeast connections between the slow anomaly and the CIR are more intense and continuous (Figure 10, cross section B1–B2) with respect to the connection of this anomaly with the SWIR, which appears neither deep nor intense (Figure 10, cross sections A1–A2 and E1–E2). These observations suggest spreading of the hot material, with the dominant direction along the northeast and the east. The thick and compact shield of the Mascarene Basin (Figure 1) appears to block the upwelling of the hot material and forces it to flow laterally up to the northeast, over the Seychelles Arc. This privileged spreading direction (Figure 10, cross section B1–B2) is in agreement with the eastward asthenospheric flow direction proposed by Forte et al. (2010) and might be influenced by the general motion toward the northeast of the overlying plate.

At 200 km in depth, the strongest slow anomaly shows two directions of expansion: (1) To the east in the northern part of Madagascar and Mozambique Channel, the slow anomaly might be connected with the slow velocity beneath the East Africa Rift (Figure 10, cross section E1–E2) and (2) to the southeast beneath South Africa (Figure 10, cross sections C1–C2 and D1-D2), where Glišović and Forte (2017) proposed a possible ancient connection with the slow velocity anomaly that originates at the core-mantle boundary.

At shallow depth (i.e., 50 km), the fast anisotropy direction beneath the Mascarene Basin shows an overall northeast direction, in agreement with the paleospreading of the area and the no net rotation general motion of the Africa Plate (absolute plate motion) (Kreemer, 2009; Seton et al., 2012). At 100 km to 150 km in depth,

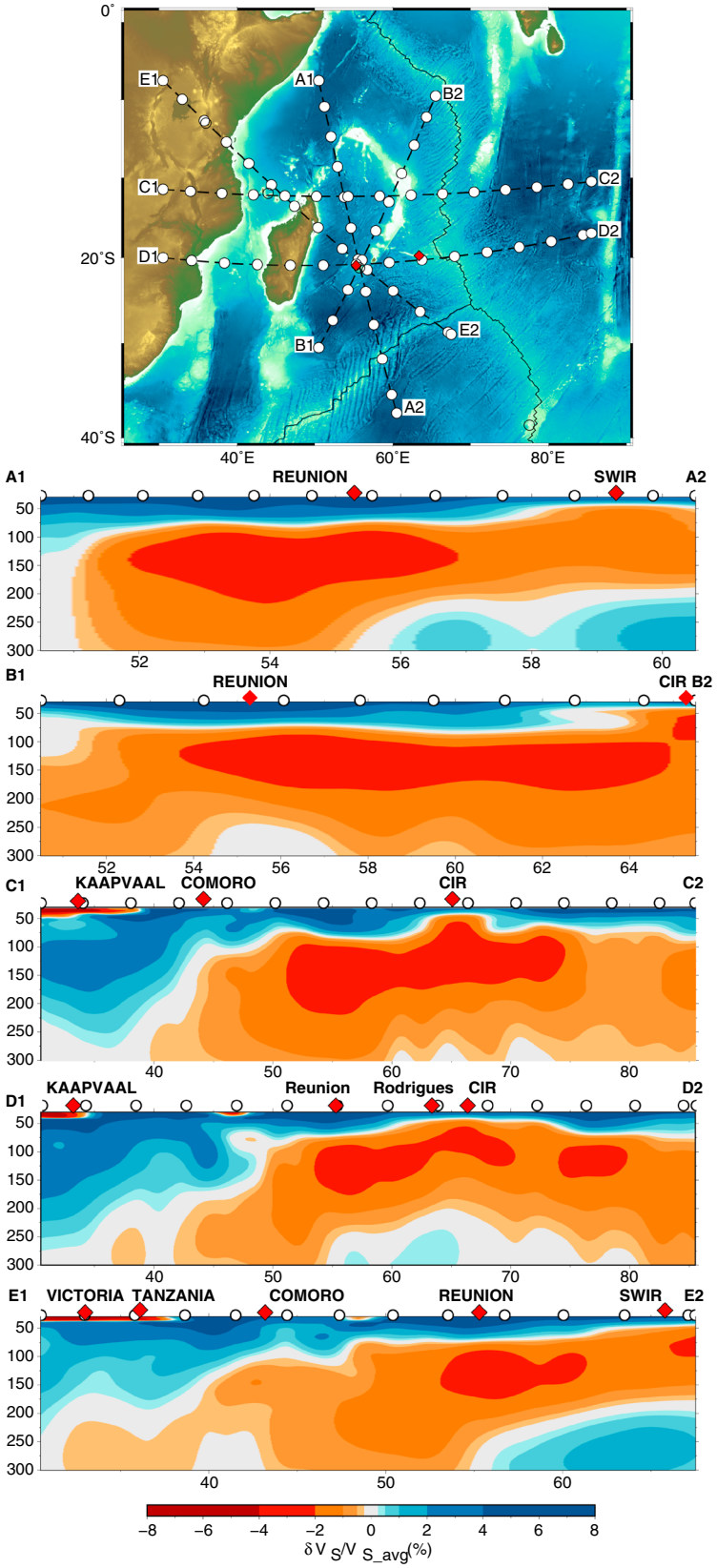

Figure 10. Vertical cross sections along great circle paths for the shear velocity distribution relative to the mean model of the area. The sections are plotted as functions of depth and latitude. Réunion and Rodrigues Islands are indicated by red diamonds, and the dotted lines show the cross sections.

the maps in Figure (8) show a significant anisotropy pattern with a well-defined NW-SE fast direction that does not correspond to the past spreading of the region nor to the general NE-SW trend that results from mantle flow models or no net rotation plate motion (Conrad & Behn, 2010; Forte et al., 2010; Kreemer, 2009). The orientation is in agreement with plate motion within the hot spot framework from HS3-Nuvel1A model (Gripp & Gordon, 2002). The difference between the anisotropy fast directions at 50 and 100 km depths might be related to the interaction at the lithosphere-asthenosphere boundary, suggesting a mechanical decoupling between the thick and old lithosphere and the underlying hot asthenospheric material characterized by slow seismic velocities.

Previous global and regional tomography studies (Burgos et al., 2014; Debayle & Lévêque, 1997; Debayle & Ricard, 2012; French & Romanowicz, 2015; Lévèque et al., 1998; Montagner, 1986b; Montagner & Jobert, 1988) have provided some evidence of slow velocity signatures in the north part of the western Indian Ocean, but they have never imaged any clear seismic evidence of the connection between the large negative anomaly in the upper mantle and the Réunion hot spot.

6.3. East Africa and Comoros Archipelago

This model also shows the velocity structure of the eastern part of the African continent. The eastern part of Tanzania and Kaapvaal cratons shows positive anomalies (+3% and +6%; Figure 8). On cross sections C1 – C2 and D1 – D2 in Figure 10, the root of the Kaapvaal craton is still visible at 250 km in depth. The Tanzania craton, which is within the eastern and western branches of the East African Rift, shows a shallow root at ∼170 km in depth, with a weak slow velocity anomaly beneath Lake Victoria (Figure 10, cross section E1 – E2). This slow anomaly (at 200 – 300 km in depth) might have been produced by convective instabilities following the edge-driven convection process due to the fast velocity structure of Tanzania adjacent to the slow velocity structures of the African rifts (King & Ritsema, 2000).

Cross sections D1 – D2 and E1 – E2 of Figure 10 show that the negative anomaly beneath Comoros Archipelago appears to be a branch of the large slow anomaly in the Indian Ocean discussed in section 6.2.

From the maps in Figure (8) (at 50 km in depth), East Africa, Mozambique Channel, and Madagascar have constant northeast azimuthal anisotropy, with the fast direction correlated with the no net rotation plate motion. Going deeper, the azimuthal anisotropy fast direction remains northeast in East Africa, but with decreasing intensity. Starting at 100 km in depth, the azimuthal pattern shows a west-east fast direction in Madagascar and Mozambique Channel, in agreement with the mantle flow, as proposed by Ghosh and Holt (2012), Behn et al. (2004), Forte et al. (2010), and Moucha and Forte (2011). The anisotropy pattern becomes more complex in the area of Comoros Islands, which appears to be due to the complex southern termination of the rift system in the area. Debate remains on the different hypotheses regarding the presence of different plumes beneath Kenya and Comoros, or a large plume whereby the slow velocity anomalies in the area might be connected (Nelson et al., 2007, 2008; Park et al., 2008; Ritsema et al., 1999), in the framework of the northern termination of the East African Rift.

Beneath the East Africa cratons (200 km in depth; Figure 10, cross sections C-D-E), the slow velocity signature continues toward the southeast beneath Comoros Islands and is connected to the large slow velocity anomaly beneath the western Indian Ocean (Figure 10, cross sections D1 – D2 and E1 – E2). This complex setting of slow velocity branches in the Comoros area suggests that the origin of the Comoros Archipelago and the seismic/volcanic activities in the region are related to a lithosphere stress that might have originated from the opening of a plate boundary (Michon, 2016), rather than plume upwelling.

7. Conclusions

We have estimated the three-dimensional *S* velocity structure around La Réunion Island down to 300 km in depth through the inversion of the fundamental mode of Rayleigh wave phase and group velocities. The availability of these data from these new OBS and land stations from the RHUM-RUM experiment enabled us to obtain a regional tomography model with finer resolution (L_r = 300 km) than previous global and regional studies. At 80 km to 100 km in depth, a slow velocity anomaly connects the negative anomaly beneath Réunion Island with the CIR. Furthermore, the fast anisotropy direction shows a west-east direction, which supports the off-axis plume-ridge distal interaction (Ito et al., 2003; Ribe et al., 2007; Schilling, 1991, 1985). The extended slow velocity anomaly beneath the north part of Mascarene Basin from 100 km to 250 km in depth might represent the source of the hot material that feeds into the Réunion hot spot.

Even though we cannot resolve the origin at depth of this anomaly, these data do not indicate a simple vertical mantle upwelling that would feed the Réunion hot spot. The tomography suggests a much more complex upwelling beneath the Mascarene Basin that interacts with the overlying lithosphere and spreads the hot material laterally over very large distances, to feed ridges and volcanic structures in the area.

Acknowledgments
The RHUM-RUM project (www.rhum-rum.net) was funded by the *Agence Nationale de la Recherche* (ANR) in France (project ANR-11-BS56-0013) and by the *Deutsche Forschungsgemeinschaft* (DFG) in Germany (grants SI1538/2-1 and SI1538/4-1). Additional support was provided by the *Centre National de la Recherche Scientifique* (CNRS) in France, the *Terres Australes et Antarctiques Françaises* (TAAF) in France, the *Institut Polaire Français Paul Emile Victor* (IPEV) in France, the Alfred Wegener Institut (AWI) in Germany, and by the EU Marie Curie CIG grant ≪ RHUM-RUM ≫ to K.S. The authors thank *Deutsche Geräte-Pool für Amphibische Seismologie* (DEPAS) in Germany, GEOMAR *Helmholtz-Zentrum f urOzeanforschung Kiel* in Germany, and the *Institut National des Sciences de l'Univers-Institut de Physique du Globe de Paris* (INSU-IPGP) in France for providing the broadband ocean bottom seismometers (DEPAS, 44; GEOMAR, 4; and INSU-IPGP, 9). The RHUM-RUM data set (https://doi.org/10.15778/RESIF.YV2011) has been assigned the FDSN network code YV and is hosted and served by the French RESIF data center (http://seismology.resif.fr). We thank C. Pequegnat and D. Wolyniec at RESIF for their continuous support in the integration, verification, and maintenance of these data and metadata at the RESIF data center. These data will be freely available by the end of 2017. The authors also thank the cruise participants and crew members on the R/V *Marion Dufresne* for cruise MD192 and on the R/V *Meteor* for cruise M101. The authors thank Wayne Crawford for his help in the data preparation. The authors also acknowledge support from discussions within TIDES COST Action ES1401 and would like to thank the whole RHUM-RUM community, and especially Kasra Hosseini for support and the constructive discussions. The following open-source tool boxes were used: GMT v.5.1.1 (Wessel et al., 2013), Python v.2.7 (Van Rossum & Drake Jr. F. L., 1995), ObsPy v.0.10.2 (Beyreuther et al., 2010), and ObspyDMT v.0.9.9b (Scheingraber et al., 2013; Hosseini, 2015). This is IPGP contribution number 3897.

References

Amante, C., & Eakins, B. W. (2009). ETOPO1 1 arc-minute global relief model: Procedures, data sources and analysis. *NOAA Technical Memorandum NESDIS NGDC-24*, *1*, 1. https://doi.org/10.7289/V5C8276M

Backus, G. E. (1970). A geometrical picture of anisotropic elastic tensors. *Reviews of Geophysics*, *8*, 633–671.

Barruol, G., & Fontaine, F. R. (2013). Mantle flow beneath La Réunion hotspot track from *SKS* splitting. *Earth and Planetary Science Letters*, *362*, 108–121.

Barruol, G., & Sigloch, K. (2013). Investigating La Réunion hotspot from crust to core. *Eos, Transactions American Geophysical Union*, *94*(23), 205–207.

Bassin, C., Laske, G., & Masters, G. (2000). The current limits of resolution for surface wave tomography in North America. *Eos, Transactions American Geophysical Union*, *81*, F897.

Behn, M. D., Conrad, C. P., & Silver, P. G. (2004). Detection of upper mantle flow associated with the African superplume. *Earth and Planetary Science Letters*, *224*, 259–274.

Beucler, E., Stutzmann, E., & Montagner, J.-P. (2003). Surface wave higher-mode phase velocity measurements using a roller-coaster-type algorithm. *Geophysical Journal International*, *155*(1), 289–307.

Beyreuther, M., Barsch, R., Krischer, L., Megies, T., Behr, Y., & Wassermann, J. (2010). Obspy: A python toolbox for seismology. *Seismological Research Letters*, *81*(3), 530–533.

Bredow, E., Steinberger, B., Gassmöller, R., & Dannberg, J. (2017). How plume-ridge interaction shapes the crustal thickness pattern of the Réunion hotspot track. *Geochemistry, Geophysics, Geosystems*, *18*, 2930–2948. https://doi.org/10.1002/2017GC006875

Burgos, G., Montagner, J.-P., Beucler, E., Capdeville, Y., Mocquet, A., & Drilleau, M. (2014). Oceanic lithosphere-asthenosphere boundary from surface wave dispersion data. *Journal of Geophysical Research*, *119*, 1079–1093. https://doi.org/10.1002/2013JB010528

Burke, K. (1996). The African Plate. *South African Journal of Geology*, *99*(4), 341–409.

Conrad, C. P., & Behn, M. D. (2010). Constraints on lithosphere net rotation and asthenospheric viscosity from global mantle flow models and seismic anisotropy. *Geochemistry, Geophysics, Geosystems*, *11*, Q05W05. https://doi.org/10.1029/2009GC002970

Courtillot, V., Davaille, A., Besse, J., & Stock, J. (2003). Three distinct types of hotspots in the Earth's mantle. *Earth and Planetary Science Letters*, *205*(3), 295–308.

Courtillot, V., Manighetti, I., Tapponnier, P., Jaupart, C., & Besse, J. (1999). On causal links between flood basalts and continental breakup. *Earth and Planetary Science Letters*, *166*, 177–195.

Courtillot, V., Besse, J., Vandamme, D., Montigny, R., Jaeger, J.-J., & Cappetta, H. (1986). Deccan flood basalts at the Cretaceous/Tertiary boundary? *Earth and Planetary Science Letters*, *80*(3–4), 361–374.

De Boor, C. (1978). *A practical guide to splines* (Vol. 27). New York: Springer.

Debayle, E., & Lévêque, J. (1997). Upper mantle heterogeneities in the Indian Ocean from waveform inversion. *Geophysical Research Letters*, *24*(3), 245–248.

Debayle, E., & Ricard, Y. (2012). A global shear velocity model of the upper mantle from fundamental and higher Rayleigh mode measurements. *Journal of Geophysical Research*, *117*, B10308. https://doi.org/10.1029/2012JB009288

Debayle, E., & Sambridge, M. (2004). Inversion of massive surface wave data sets: Model construction and resolution assessment. *Journal of Geophysical Research*, *109*, B02316. https://doi.org/10.1029/2003JB002652

Debayle, E., Dubuffet, F., & Durand, S. (2016). An automatically updated *S*-wave model of the upper mantle and the depth extent of azimuthal anisotropy. *Geophysical Research Letters*, *43*, 674–682. https://doi.org/10.1002/2015GL067329

Duncan, R. A., & Hargraves, R. B. (1990). $^{40}Ar/^{39}$ Ar geochronology of basement rocks from the Mascarene Plateau, the Chagos Bank, and the Maldive Ridge. In R. A. Duncan, et al. (Eds.), *Proceedings of the Ocean Drilling Program, Scientific Results* (Vol. 115, pp. 43–51). Collage Station, TX: Ocean Drilling Programme.

Duncan, R. A., Backman, J., & Peterson, L. C. (1990). The volcanic record of the reunion hotspot. In R. A. Duncan, et al. (Eds.), *Proceedings of the Ocean Drilling Program, Scientific Results* (Vol. 115, pp. 3–10). Collage Station, TX: Ocean Drilling Programme.

Dyment, J., Lin, J., & Baker, E. T. (2007). Ridge-hotspot interactions: What mid-ocean ridges tell us about deep Earth processes. *Oceanography*, *20*(1), 102–115.

Dziewonski, A. M., & Anderson, D. L. (1981). Preliminary reference Earth model. *Physics of the Earth and Planetary Interiors*, *25*, 297–356.

Efron, B., & Tibshirani, R. (1991). Statistical data analysis in the computer age (Tech. Rep. 379). Stanford, CA: Department of Statistics, University of Toronto.

Fontaine, F. R., Barruol, G., Tkalčić, H., Wölbern, I., Rümpker, G., Bodin, T., & Haugmard, M. (2015). Crustal and uppermost mantle structure variation beneath La Réunion hotspot track. *Geophysical Journal International*, *203*(1), 107–126.

Forte, A. M., Quéré, M. S., Moucha, R., Simmons, N. A., Grand, S. P., Mitrovica, J. X., & Rowley, D. B. (2010). Joint seismic-geodynamic-mineral physical modeling of African geodynamics: A reconciliation of deep-mantle convection with surface geophysical constraints. *Earth and Planetary Science Letters*, *295*, 329–341. https://doi.org/10.1016/j.epsl.2010.03.017

French, S. W., & Romanowicz, B. (2015). Broad plumes rooted at the base of the Earth's mantle beneath major hotspots. *Nature*, *2*, 3. https://doi.org/10.1038/nature14876

Georgen, J. E., Lin, J., & Dick, H. J. (2001). Evidence from gravity anomalies for interactions of the Marion and Bouvet hotspots with the Southwest Indian Ridge: Effects of transform offsets. *Earth and Planetary Science Letters*, *187*(3), 283–300.

Ghosh, A., & Holt, W. E. (2012). Plate motions and stresses from global dynamic models. *Science*, *335*(6070), 838–843.

Glišović, P., & Forte, A. M. (2017). On the deep-mantle origin of the Deccan Traps. *Science*, *355*(6325), 613–616.

Gripp, A. E., & Gordon, R. G. (2002). Young tracks of hotspots and current plate velocities. *Geophysical Journal International*, *150*(2), 321–361.

Haned, A., Stutzmann, E., Schimmel, M., Kiselev, S., Davaille, A., & Yelles-Chaouche, A. (2016). Global tomography using seismic hum. *Geophysical Journal International*, *204*(2), 1222–1236.

Hofmann, A. (1997). Mantle geochemistry: The message from oceanic volcanism. *Nature*, *385*(6613), 219–229.

Hosseini, K. (2015). ObspyDMT (Version 1.0.0) [Software].

Ito, G., Lin, J., & Graham, D. (2003). Observational and theoretical studies of the dynamics of mantle plume-mid-ocean ridge interaction. *Reviews of Geophysics*, *41*(4), 1017. https://doi.org/10.1029/2002RG000117

Kanamori, H., & Given, J. W. (1981). Use of long-period surface waves for rapid determination of earthquake-source parameters. *Physics of the Earth and Planetary Interiors*, *27*(1), 8–31.
King, S. D., & Ritsema, J. (2000). African hot spot volcanism: Small-scale convection in the upper mantle beneath cratons. *Science*, *290*(5494), 1137–1140.
Kreemer, C. (2009). Absolute plate motions constrained by shear wave splitting orientations with implications for hot spot motions and mantle flow. *Journal of Geophysical Research*, *114*, B10405. https://doi.org/10.1029/2009JB006416
Laske, G., Masters, G., Ma, Z., & Pasyanos, M. (2013). Update on CRUST1.0 a 1-degree global model of Earth's crust. *Geophysical Research Abstract*, *15*, 2658.
Lévèque, J., Debayle, E., & Maupin, V. (1998). Anisotropy in the Indian Ocean upper mantle from Rayleigh and Love waveform inversion. *Geophysical Journal International*, *133*(3), 529–540.
Levshin, A. (1985). Effects of lateral inhomogeneities on surface wave amplitude measurements. *Annales Geophysicae*, *3*(4), 511–518.
Mahoney, J. J., Natland, J. H., White, W. M., Poreda, R., Bloomer, S. H., & Baxter, A. N. (1989). Isotopic and geochemical provinces of the western Indian Ocean spreading centers. *Journal of Geophysical Research*, *94*, 4033–4052.
Mahoney, J. J., Natland, J. H., White, W. M., Poreda, R., Bloomer, S. H., Fisher, R. L., & Baxter, A. N. (1989). Isotopic and geochemical provinces of the western Indian Ocean spreading centers. *Journal of Geophysical Research*, *94*(B4), 4033–4052. https://doi.org/10.1029/JB094iB04p04033
McDougall, I. (1965). A geological reconnaissance of Rodriguez Island, Indian Ocean. *Nature*, *206*, 26–27.
Michon, L. (2016). The volcanism of the Comoros archipelago integrated at a regional scale. In *Active volcanoes of the southwest Indian Ocean* (pp. 333–344). Berlin: Springer.
Montagner, J.-P. (1986a). Regional three-dimensional structures using long-period surface waves. *Annales Geophysicae*, *4*(B3), 283–294.
Montagner, J.-P. (1986b). 3-dimensional structure of the Indian Ocean inferred from long period surface waves. *Geophysical Research Letters*, *13*(4), 315–318.
Montagner, J.-P., & Jobert, N. (1988). Vectorial tomography—II. Application to the Indian Ocean. *Geophysical Journal International*, *94*(2), 309–344.
Montagner, J.-P., & Nataf, H.-C. (1986). A simple method for inverting the azimuthal anisotropy of surface waves. *Journal of Geophysical Research*, *91*(B1), 511–520.
Morgan, W. J. (1971). Convection plumes in the lower mantle. *Nature*, *230*(5288), 42–43.
Morgan, W. J. (1978). Rodrigues, Darwin, Amsterdam, . . . , a second type of hotspot island. *Journal of Geophysical Research*, *83*(B11), 5355–5360.
Moucha, R., & Forte, A. M. (2011). Changes in African topography driven by mantle convection. *Nature Geoscience*, *4*(10), 707–712.
Nataf, H.-C. (2000). Seismic imaging of mantle plumes. *Annual Review of Earth and Planetary Sciences*, *28*(1), 391–417.
Nelson, W., Furman, T., van Keken, P., & Lin, S. (2007). Two plumes beneath the East African Rift system: A geochemical investigation into possible interactions in Ethiopia. *AGU Fall Meeting Abstracts*, *1*, 04.
Nelson, W., Furman, T., & Hanan, B. (2008). Sr, Nd, Pb and Hf evidence for two-plume mixing beneath the East African Rift System. *Geochimica et Cosmochimica Acta*, *72*, A676.
Nougier, J., Cantagrel, J., & Karche, J. (1986). The comores archipelago in the western Indian Ocean: Volcanology, geochronology and geodynamic setting. *Journal of African Earth Sciences (1983)*, *5*(2), 135–144.
Park, Y., Nyblade, A. A., Rodgers, A. J., & Al-Amri, A. (2008). *S* wave velocity structure of the Arabian Shield upper mantle from Rayleigh wave tomography. *Geochemistry, Geophysics, Geosystems*, *9*, Q07020. https://doi.org/10.1029/2007GC001895
Pratt, M. J., Wysession, M. E., Aleqabi, G., Wiens, D. A., Nyblade, A. A., Shore, P., . . . Rindraharisaona, E. (2017). Shear velocity structure of the crust and upper mantle of Madagascar derived from surface wave tomography. *Earth and Planetary Science Letters*, *458*, 405–417.
Press, W. H., Teukolsky, S. A., Vetterling, W. T., & Flannery, B. P. (1992). *Numerical recipes in Fortran 77* (Vol. 1). New York: Press Syndicate of the University of Cambridge.
Ribe, N., Davaille, A., & Christensen, U. (2007). Fluid dynamics of mantle plumes. In J. R. R. Ritter & U. R. Christensen (Eds.), *Mantle Plumes* (pp. 1–48). Berlin: Springer.
Ritsema, J., van Heijst, H. J., & Woodhouse, J. H. (1999). Complex shear wave velocity structure imaged beneath Africa and Iceland. *Science*, *286*(5446), 1925–1928.
Saito, M. (1988). Disper80: A subroutine package for the calculation of seismic normal mode solutions. In D. Doornbos (Ed.), *Seismological algorithms: Computational methods and computer programs* (pp. 293–319). New York: Academic Press.
Sambridge, M., Bodin, T., Gallagher, K., & Tkalčić, H. (2013). Transdimensional inference in the geosciences. *Philosophical Transactions of the Royal Society A*, *371*(1984), 20110547.
Schaeffer, A., & Lebedev, S. (2013). Global shear speed structure of the upper mantle and transition zone. *Geophysical Journal International*, *194*, 417–449.
Scheingraber, C., Hosseini, K., Barsch, R., & Sigloch, K. (2013). Obspyload: A tool for fully automated retrieval of seismological waveform data. *Seismological Research Letters*, *84*(3), 525–531.
Schilling, J.-G. (1973). Iceland mantle plume: Geochemical study of Reykjanes Ridge. *Nature*, *242*, 565–571.
Schilling, J.-G. (1985). Upper mantle heterogeneities and dynamics. *Nature*, *314*, 62–67.
Schilling, J.-G. (1991). Fluxes and excess temperatures of mantle plumes inferred from their interaction with migrating mid-ocean ridges. *Nature*, *352*, 397–403.
Scholz, J.-R., Barruol, G., Fontaine, F. R., Sigloch, K., Crawford, W. C., & Deen, M. (2017). Orienting ocean-bottom seismometers from *P*-wave and Rayleigh wave polarizations. *Geophysical Journal International*, *208*(3), 1277–1289.
Scholz, J.-R., Barruol, G., Fontaine, F. R., Montagner, J.-P., Stutzmann, E., Sigloch, K., & Mazzullo, A. (2016). *Upper mantle seismic anisotropy in the southwest Indian Ocean from SKS-splitting measurements: Plate, plume and ridges signatures*. Paper presented at AGU Fall Meeting Abstracts S33F-06. San Francisco, CA.
Seton, M., Müller, R., Zahirovic, S., Gaina, C., Torsvik, T., Shephard, G., . . . Chandler, M. (2012). Global continental and ocean basin reconstructions since 200 Ma. *Earth-Science Reviews*, *113*(3), 212–270.
Sheth, H. (1999). Flood basalts and large igneous provinces from deep mantle plumes: Fact, fiction, and fallacy. *Tectonophysics*, *311*(1), 1–29.
Sleep, N., Ebinger, C., & Kendall, J.-M. (2002). Deflection of mantle plume material by cratonic keels. *Geological Society, London, Special Publications*, *199*(1), 135–150.
Smith, M. L., & Dahlen, F. (1973). The azimuthal dependence of Love and Rayleigh wave propagation in a slightly anisotropic medium. *Journal of Geophysical Research*, *78*(17), 3321–3333.
Stähler, S. C., Sigloch, K., Hosseini, K., Crawford, W. C., Barruol, G., Schmidt-Aursch, M., . . . Deen, M. (2016). Performance report of the RHUM-RUM ocean bottom seismometer network around La Réunion, western Indian Ocean. *Advances in Geosciences*, *41*, 43–63.

Storey, B. C. (1995). The role of mantle plumes in continental breakup: Case histories from Gondwanaland. *Nature*, *377*(6547), 301–308.
Stutzmann, E., & Montagner, J.-P. (1993). An inverse technique for retrieving higher mode phase velocity and mantle structure. *Geophysical Journal International*, *113*(3), 669–683.
Tarantola, A., & Valette, B. (1982). Generalized nonlinear inverse problems solved using the least squares criterion. *Reviews of Geophysics*, *20*(2), 219–232.
Thoraval, C., Tommasi, A., & Doin, M.-P. (2006). Plume-lithosphere interaction beneath a fast moving plate. *Earth and Planetary Science Letters*, *33*, 1–4.
Upton, B. G. J. (1980). *The Comores archipelago* (Vol. 6, pp. 21–24). New York: Press.
Van Rossum, G., & Drake, Jr. F. L. (1995). *Python reference manual*. Amsterdam: Centrum voor Wiskunde en Informatica.
Wessel, P., Smith, W. H., Scharroo, R., Luis, J., & Wobbe, F. (2013). Generic Mapping Tools: Improved version released. *Eos, Transactions American Geophysical Union*, *94*(45), 409–410.
Woodhouse, J. (1974). Surface waves in a laterally varying layered structure. *Geophysical Journal International*, *37*(3), 461–490.
Wysession, M., Wiens, D., Nyblade, A., & Rambolamanana, G. (2012). *Investigating mantle structure with broadband seismic arrays in Madagascar and Mozambique*. Paper presented at AGU Fall Meeting Abstracts. Abstract T31B - 2591.
Yamamoto, M., Morgan, J. P., & Morgan, W. J. (2007a). Global plume-fed asthenosphere flow—I: Motivation and model development. *Geological Society of America Special Papers*, *430*, 165–188.
Yamamoto, M., Morgan, J. P., & Morgan, W. J. (2007b). Global plume-fed asthenosphere flow—II: Application to the geochemical segmentation of mid-ocean ridges. *Geological Society of America Special Papers*, *430*, 189–208.